Study of Polarization Differences in K_u-Band Ocean Radar Imagery

ANDRE V. SMIRNOV AND VALERY U. ZAVOROTNY

Cooperative Institute for Research in Environmental Sciences, University of Colorado/NOAA, Boulder, Colorado

(Manuscript received 27 September 1993, in final form 11 November 1994)

ABSTRACT

Radar returns from the sea surface can be represented as the sum of two contributions from Bragg scattering and from individual breaking events. This representation is used to analyze polarimetric radar images of ocean areas obtained at grazing angles $6° < \psi < 18°$ with the airborne K_u-band radar in the New York Bight. All images were obtained for light and moderate winds and can be divided into three types according to texture differences. Images obtained confirm that there are differences between returns for horizontal/horizontal (HH) and vertical/vertical (VV) polarizations for the three types. The first type agrees qualitatively with predictions of the two-scale Bragg model, whereas the other two do not. The second and third types have a significant spike contribution from breaking events at both polarizations. The last type reveals drastic differences between images obtained using HH and VV polarizations. The polarization dissimilarity is a result of a low correlation between the spike clusters in HH-polarized images and the variations of continuous background in VV-polarized images. The role of atmospheric stability in processes responsible for spatial decorrelation of the different scatterers is also examined.

1. Introduction

The microwave airborne real-aperture radar (RAR) and the synthetic-aperture radar (SAR) are capable of obtaining practically synchronous radio images of vast ocean areas with high resolution, thus making these techniques unique for global ocean monitoring. The RAR image intensity is related to the ocean scene by a transfer function that can be determined for the various scattering mechanisms (i.e., Bragg, specular, etc.). Alpers et al. (1981) calculated linear transfer functions using the two-scale model and applied them to a description of the imaging process. This approach yields no drastic polarization differences for images of ripples tilt modulated with long gravity waves. This and other theoretical approaches based on the two-scale tilt-modulation model are limited by angles of incidence from about 20° to 70°. Usually, typical RAR systems operate within these limits. However, there is a range of angles, $\theta > 70°$, where the signal behavior cannot be explained merely by Bragg scattering. Another component, so-called radar sea spikes, reveals itself in low-grazing-angle observations (Trizna 1991).

Phillips (1988) discussed relative contributions to radar sea returns from Bragg scattering on ocean ripples and from sea spikes produced by breaking waves at radio bands from X to P. He introduced in his theoretical model a scaling parameter that includes wind friction velocity. When this parameter exceeds about 2, the behavior of the backscattered cross section becomes very spiky because of the surface roughness produced by individual breaking waves. For radar remote sensing purposes, one can take advantage of the sea spike returns rather than to try to suppress them, especially in the ocean radar imagery.

We present some results and interpretation of the K_u-band RAR imagery performed during the 1992 Joint U.S.–Russia Internal Wave Remote Sensing Experiment. The instrumentation and environmental conditions are discussed in section 2. RAR images of the ocean surface in the New York Bight, obtained at large incident angles $72° < \theta < 84°$ (or, respectively, under small grazing angles $6° < \psi = 90° - \theta < 18°$) with sea states from low to moderate, reveal a more diverse picture than that predicted by linear modulation theory based on the two-scale model. The main experimental results and analysis of two-polarization images are given in sections 3 and 4. It was found that the sea spikes play an important role in RAR imagery even under such low and moderate wind conditions. Moreover, the visual difference between horizontal/horizontal (HH) and vertical/vertical (VV) polarized images, if it appears, is produced by strong spike clusters in HH-polarized images. Therefore, using only the Bragg mechanism fails to explain these results. To be precise, the sea state in this experiment cannot be described as simply low or moderate; a more detailed classification of sea surface conditions is suggested. The sea surface conditions need to be characterized by such features as

Corresponding author address: Dr. Andre V. Smirnov, Ocean Remote Sensing Division, NOAA/ERL/CIRES, 325 Broadway, Boulder, CO 80303-3328.

steepening, sharpening, and breaking of waves. Breakers not only occur during high sea states, but these events are also found to correlate with an unstable atmospheric stratification near the sea surface and with relatively light winds.

2. Experiment

a. The instrumentation

The joint U.S.–Russia Internal Wave Remote Sensing Experiment took place from 12 to 25 July 1992 on the continental shelf off the East Coast of the United States in the New York Bight region used for the SAR Internal Wave Signature Experiment in 1984 (Gasparovic et al. 1988). The surrounding area was studied with instruments on a Russian research vessel, the *Academic Ioffe,* on a moored spar buoy with meteorological and wave sensors from The Johns Hopkins University/Applied Physics Laboratory (JHU/APL), and on aircraft equipped with RAR (the Russian TU-134 aircraft) and with SAR (the NASA/Jet Propulsion Laboratory DC-8 aircraft). The main working area for the ship and aircraft was near the moored spar buoy at 40°10.78′N, 71°56.36′W (Fig. 1). In this paper Eastern Daylight Time (EDT) is used, which is 4 hours earlier than Universal Time (UTC). The basic airborne RAR imagery technique has been described previously (Lavrova et al. 1991; Smirnov and Yakovlev 1992). Here we define the radar image of a wavy surface as the two-dimensional signal $I(r)$, which is proportional to the energy of radio waves at a specific polarization and at the radar operating frequency, scattered by a surface within the radar footprint, received by the radar antenna, and integrated over the registration time. The geometry of the experiment is presented in Fig. 2. During the experiment the airborne radar with a peak power of 60 kW, a 2-kHz pulse repetition frequency, and a 110-ns transmitted pulse width, worked in the K_u-band frequency ($\lambda = 2.25$ cm). Two cylindrical antennas (6 m × 0.44 m), one on each side of the aircraft, were used alternately for transmitting and receiving HH and VV signals. The HH signal is the horizontally transmitted and received component, which is perpendicular to the plane of incidence, and VV is the vertically transmitted and received component, which is in the plane of incidence. Each pulse at the HH polarization is followed by a pulse at the VV polarization. Therefore, the pulse repetition frequency for each polarization was 1 kHz. The antenna footprint was about 25 m × 25 m for the grazing angle $\psi = 18°$. The broad beamwidth in the elevation plane (~10°), and the narrow azimuthal beamwidth ($\theta_b = 0.2°$) of the transmitter–receiver antenna, enabled us to obtain radar images of a sea surface over the 15-km swath band from each side of the aircraft, with a ground separation of 12.4 km between the left and right swaths at the nominal 2-km aircraft altitude. The radar echoes from each transmitted pulse were square law detected, log amplified, and digitized. The returned power was digitized to 8 bits and stored in the fast buffer memory of the onboard computer (Smirnov and Yakovlev 1992). The digital signal in each cell along the range is accumulated from the number of pulses required to fly 25 m along the flight direction (from 150 to 230 pulses). This number depends on the aircraft's speed. The number of pixels along the range was constant and composed of 506 points; the pixel width was 25 m for each range cell. The digitized swath band was 12.8 km and started from the minimum slant range of 6.5 km. The grazing angles ψ within the swath band varied from 6° to 18°. There was an angular difference of about 1.2° in the azimuthal plane between the beams for the two polarizations. Each of the eight mapping flights conducted during the experiment consisted of up to four swaths with a length of about 60 km, which were oriented both along the isobaths and across them toward the open ocean.

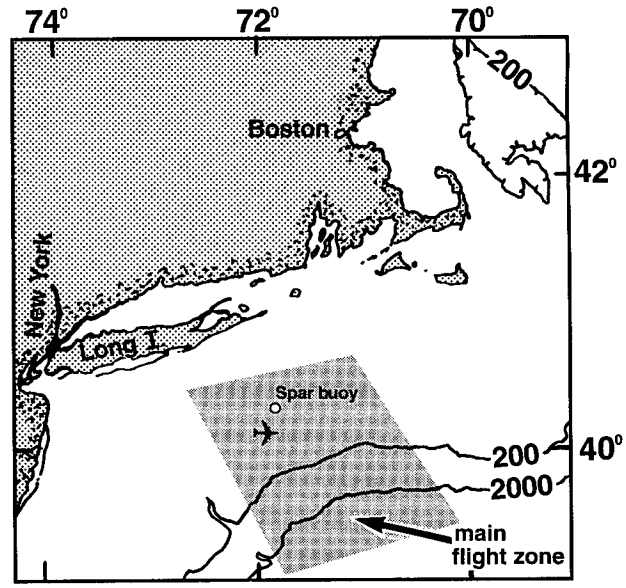

FIG. 1. Location of the experiment in the New York Bight in July 1992 and the main flight zone. Bathymetric contours are in meters.

b. Environmental conditions

Environmental measurements were made from the *Academic Ioffe* and from the spar buoy. Meteorological data are recorded routinely on the vessel and buoy. Measurements using the ship's facilities can be briefly described as a combination of measurements of air temperature at a height of about 20 m, surface water temperature and salinity, atmospheric pressure and relative humidity, and wind speed and direction at a height near 30 m. The same meteorological measurements were made on the buoy at a height of 2 m. This buoy meteorological equipment was designed by JHU/APL. Table 1 shows all meteorological data obtained and

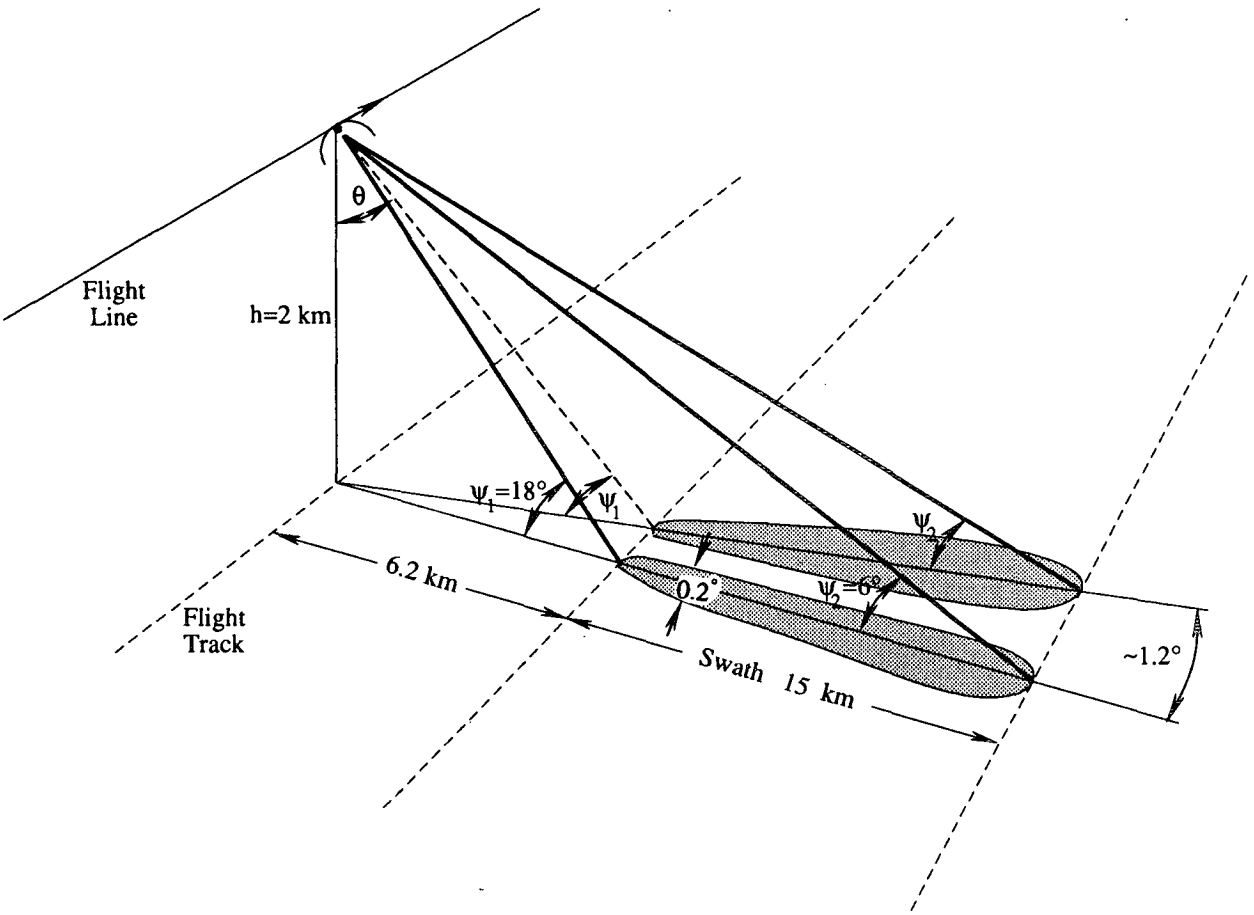

FIG. 2. Geometry of the surface illumination to the right side of the aircraft, and the geometric discrepancy between HH and VV footprints.

also the values of significant wave height (SWH) recorded by the wave sensors on the spar buoy. During the experiment, balloon-launched radiosondes were used to record atmospheric variables from sea level to heights of 3–6 km. Launches were made from the ship twice daily on the days and near the time of aircraft flights.

In situ measurements were made in July 1992 for different wind and wave conditions but there were no strong winds. Figures 3a–d present the time distribution of the atmospheric variables. The times (on 16, 21, and 24 July) chosen for analysis of three cases of the radar data are marked by vertical lines in Fig. 3. As shown in Fig. 3a, the wind speed varied from light to

TABLE 1. Times of observations of different types of radar images and corresponding environmental conditions: type 1, large-scale textures of the HH and VV images are similar; type 2, polarization differences between HH and VV images are not significant; type 3, textures between HH and VV images are totally or partially different.

Date (July 1992)	Time (EDT)	Wind direction	Wind speed ($m\ s^{-1}$)	SWH (m)	Sea–air temperature difference (°C)	Type of radar image
15	1650–1730	SWW	6	0.75	−1	1
16	1430–1610	NE	10	0.85	2	2–3
18	1030–1200	SW	8	0.75	−1	2–3
19	0850–1030	SWW	6	0.6	0	1
21	1050–1210	SSW	7.5	0.75	0.5	1
24	1235–1410	NE	7.5	1	3	3
24	1800–1850	NE	8	1.05	3	3
24	2235–2340	NEE	7.5	1.05	3	3

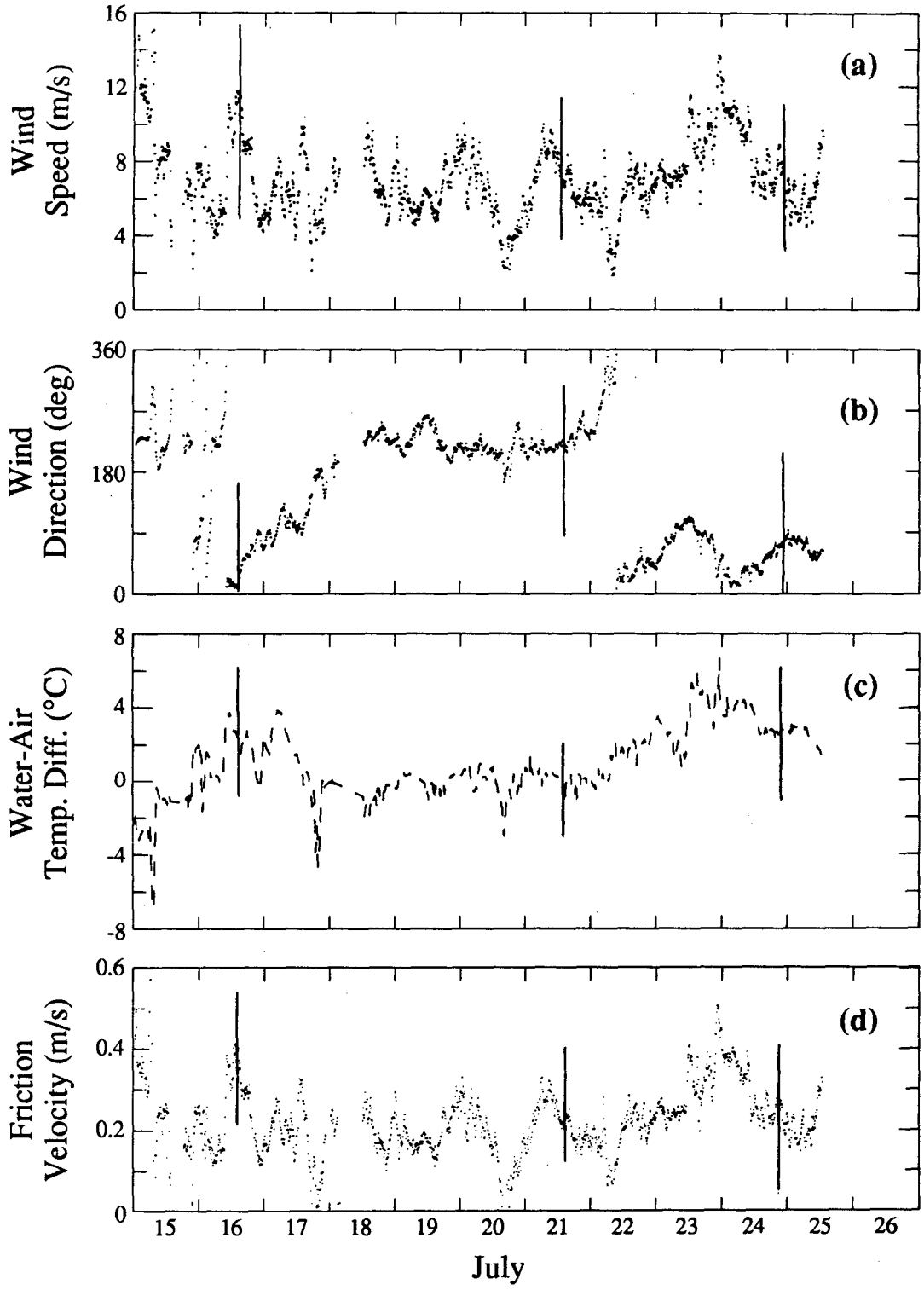

FIG. 3. Time series of shipboard meteorological measurements: (a) wind speed (m s^{-1}); (b) wind direction (degrees); (c) water − air temperature difference (°C); (d) friction velocity (m s^{-1}), evaluated from measurements. The vertical lines indicate times chosen for analysis of radar data.

moderate. During the aircraft flights wind speeds were 6–8 m s^{-1} except on 16 July when the recorded wind speed was about 11 m s^{-1}. According to Figs. 3b and 3c, the positive difference of water–air temperatures can be correlated with northeast–east winds, and the near-zero difference of the water–air temperature with south-southwest winds.

c. *Wind friction velocity*

The maxima in friction velocity (Fig. 3d) correspond to the highest wind speeds (16 and 23 July). The friction velocity u_* is computed according to Monin–Obukhov similarity theory:

$$u_* = \frac{\kappa U}{\ln \frac{z}{z_0} - \Psi_m}, \qquad (1)$$

where κ is the von Kármán constant, Ψ_m is the nondimensional stability parameter that is a function of the bulk Richardson number, z_0 is the roughness parameter, and U is given by $U = \sqrt{U_z^2 + U_c^2}$, where U_z is the measured wind speed at height z and U_c is a "convective velocity" (Anthes et al. 1987), which is important under conditions of low mean wind speed and unstable conditions, $U_c = C\sqrt{\theta_s - \theta_z}$ for $\theta_s \geq \theta_z$, $U_c = 0$ for $\theta_s < \theta_z$, where $C = 2$ and is expressed in units of m s^{-1} $K^{-1/2}$, and θ_s and θ_z are potential temperatures at the sea surface and height z.

3. Results of the experiment

Images obtained in the experiment contain internal wave signatures, which we utilized as common features for referencing the images at two polarizations, although the study of surface roughness changes induced by internal waves was beyond the scope of this work. The texture differences in the images were classified by dividing all pairs of the two-polarization RAR images into three categories, or types. Table 1 contains the data about the occurrences of the different types of RAR images, together with data for corresponding environmental conditions.

For images of the first type (e.g., about 1145 EDT 21 July) the large-scale textures of the HH image and the VV image are similar, as shown in Fig. 4. The figure shows the radar images at two polarizations for an area of 9.5 km × 9.5 km. The arrow in Figs. 4, 6, and 7 indicates the radar beam direction, and the aircraft symbol shows the aircraft heading. A typical range run of the radar image brightness is presented in Fig. 5a. The mean brightness of the HH image is much less than the mean brightness of the VV image, but the image contrast is greater for the HH image. The sea state was estimated to be calm or moderate by means of in situ measurements. Such situations made up approximately 40% of the total observation time in the experiment. The stable near-surface atmospheric stratification, namely, a positive temperature gradient in the near-water atmospheric layer, occured during these observations.

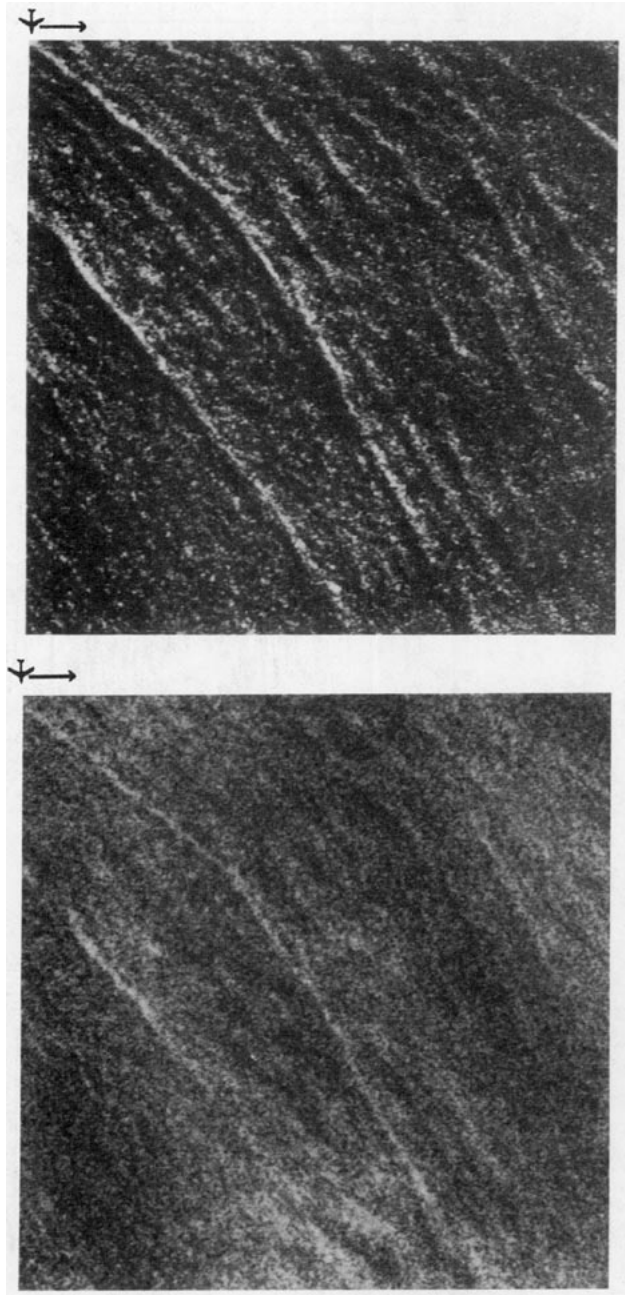

FIG. 4. Radar images of the first type of the ocean surface, obtained at 1145 EDT 21 July for a 9.5 km × 9.5 km area: (a) HH polarization and (b) VV polarization. The arrow indicates the radar beam direction, and the aircraft symbol shows the aircraft heading.

All images with both horizontal and vertical polarizations contain "spikes," regions of bright bursts, or target-like spots with a size of about two pixels. Some of the spikes are randomly scattered (see the bottom left corner of Fig. 4a); others are combined into fea-

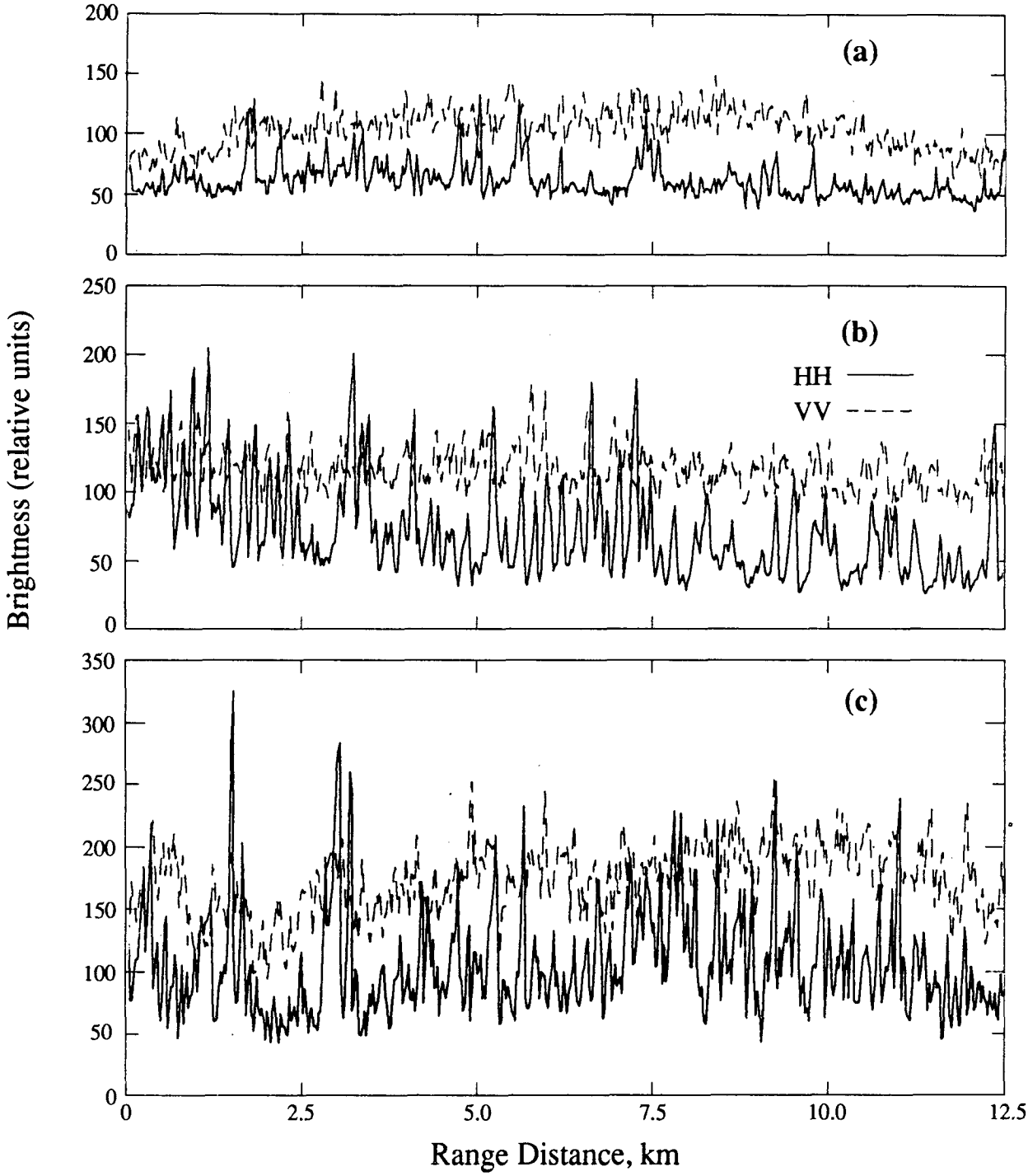

FIG. 5. Typical HH range (solid) and VV range (dashed) distributions of radar image brightness for different types of RAR images: (a) the first type, (b) the second type, and (c) the third type.

tures (e.g., see the linear feature in Fig. 4a along the main diagonal). Spikes in the images of the first type exist in regions where the surface wave spectrum has been disturbed beyond equilibrium through straining by currents induced by internal waves.

Images of the second type (e.g., about 1550 EDT 16 July) do not have significant polarization differences in either mean brightness or image contrast (Fig. 6). These images represent a rather homogeneous background with a considerable number of randomly dis-

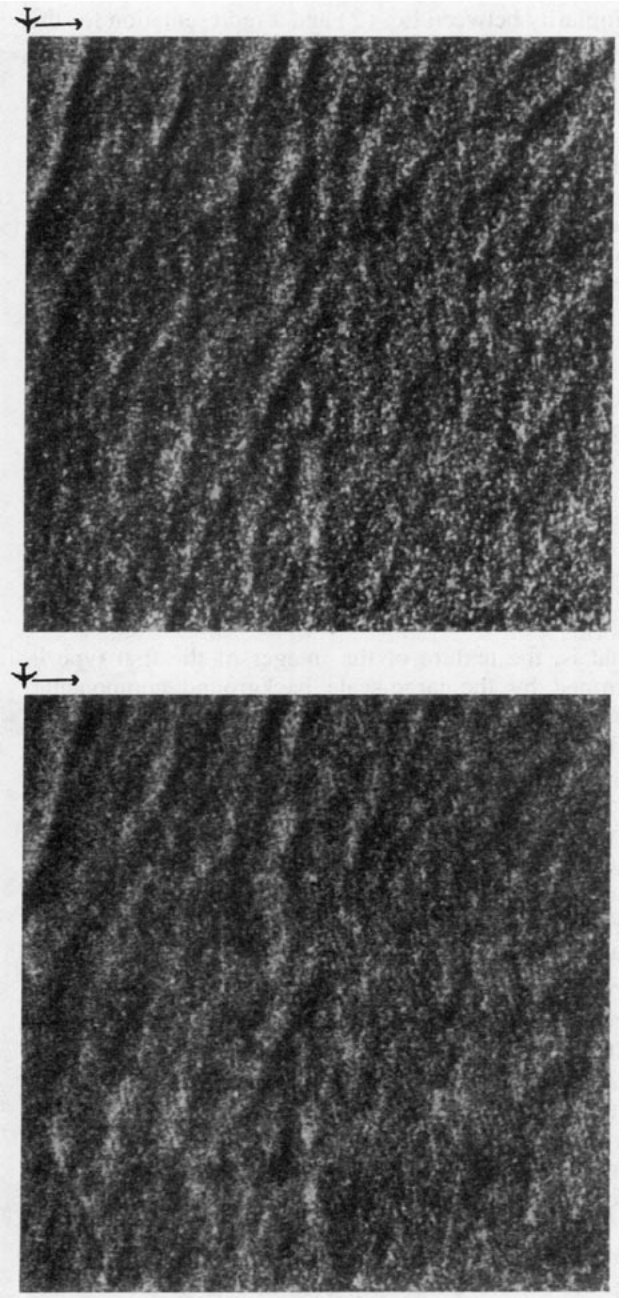

FIG. 6. Radar images of the second type of ocean surface obtained at 1550 EDT 16 July for a 9.5 km × 9.5 km area: (a) HH polarization and (b) VV polarization.

tributed spikes. A typical range run of the radar image brightness is presented in Fig. 5b. A comparison with in situ measurements of sea state shows that the images of the second type correspond to the highest sea states that occurred in the experiment, with wind speed about 10 m s^{-1}. As scatterometric measurements show (Guinard et al. 1971), under these conditions the average backscattering cross section at the HH polarization begins to exceed the corresponding theoretical values for grazing angles $\psi < 30°$ and may reach the level of the average backscattering cross section at the VV polarization for stormy conditions. However, stormy conditions were not present during the New York Bight experiment. Situations that correspond to the second type of RAR images made up less than 10% of the total observations and were under conditions of neutral near-surface atmospheric stratification.

The main focus is on images of the third type (e.g., about 2245 EDT 24 July). They are characterized by a total or partial lack of coincidence between the textures (patterns) at different polarizations (see an example of such images in Fig. 7). The presence of spikes in these images (mainly in the HH images) is significant and dominant. Moreover, the HH images are represented by some kind of spike clusters. A typical range run of the radar image brightness is presented in Fig. 5c. Situations where images of the third type occurred made up approximately 50% of the observations. The sea state was, surprisingly, not very high (see Fig. 2a). However, another interesting circumstance took place: an unstable atmospheric stratification (a negative temperature gradient in the near-water atmospheric layer). It appears that this circumstance plays an important role in the occurrence of the HH–VV differences in RAR images of the third type.

4. Analysis of two-polarization RAR imaging

a. Texture peculiarities of two-polarization images

There are important differences between conventional scatterometric measurements and measurements using high spatiotemporal resolution radars. In the former case, because of the long integration time and large footprints, the behavior of the resulting signal is closer to the theoretical description that uses the mean value of the backscattering cross section. When the radar footprint and the integration time get smaller and smaller, the fluctuating component of the signal starts to manifest itself.

With the mean speed of an airplane of 130 m s^{-1}, the time interval needed to accumulate a signal for one pixel in the image was about 0.2 s. It is clear that this is enough time to average only the very fast fluctuating component of the signal. Bursts of the return signal separated with a time interval longer than 0.2 s were not averaged and produced resolved sea spikes. Remarkably, almost all images (Figs. 4, 6, and 7) contain spikes that differ only in amplitude and spatial distribution, depending on the image type and the signal polarization (cf. Figs. 5a–c).

Let us denote the brightness of the image of the ith type as a function $H_i(\mathbf{r})$ for the HH polarization and as a function $V_i(\mathbf{r})$ for the VV polarization. They can be represented as the sums

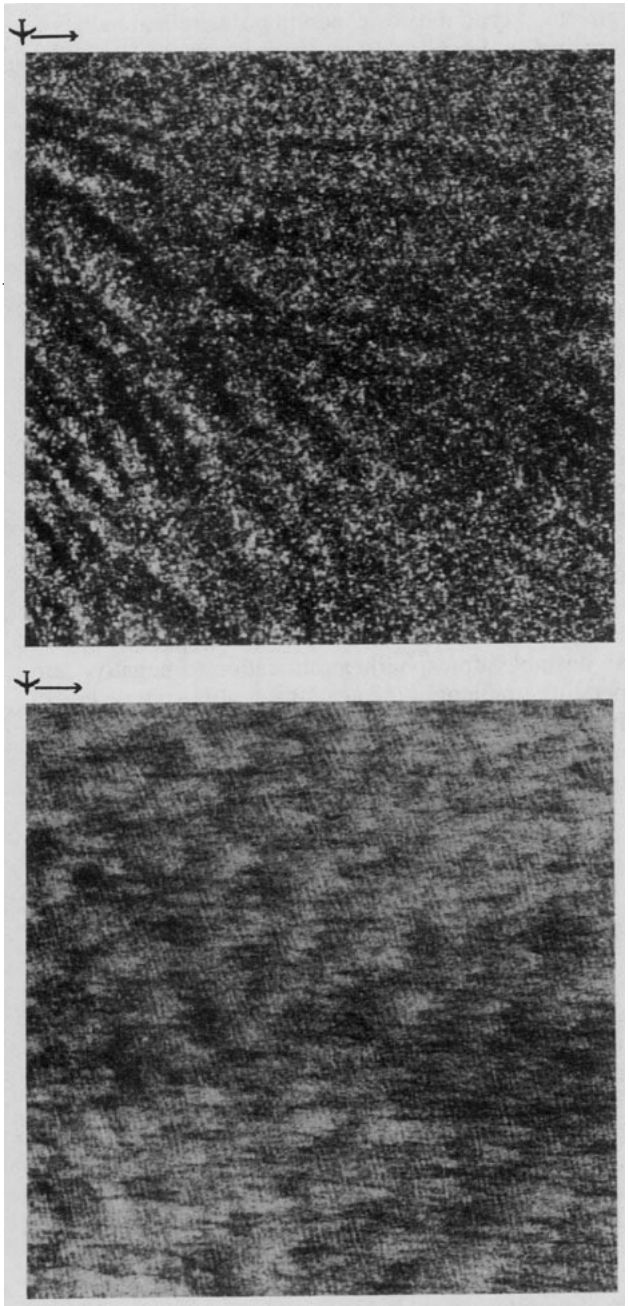

FIG. 7. Radar images of the third type of ocean surface obtained at 2245 EDT 24 July for a 9.5 km × 9.5 km area: (a) HH polarization and (b) VV polarization.

$$H_i(\mathbf{r}) = B_i^H(\mathbf{r}) + S_i^H(\mathbf{r}),$$
$$V_i(\mathbf{r}) = B_i^V(\mathbf{r}) + S_i^V(\mathbf{r}), \qquad (2)$$

where B_i and S_i are, respectively, the mean large-scale background component and the small-scale spike component of the image brightness. The radius vector $\mathbf{r}$ has an azimuthal coordinate x and a range coordinate y. Upper indices stand for the polarizations. There is some similarity between Eq. (2) and a representation for the normalized backscattering cross section, σ_0, introduced by Phillips (1988). He assumed that $\sigma_0 = \sigma_B + \sigma_{SS}$, where σ_B is the Bragg backscattering cross section and σ_{SS} is the total cross section produced by breaking at all scales, that is, the sea spike contribution. Actually, whether Eq. (2) is equal to the equation $\sigma_0 = \sigma_B + \sigma_{SS}$ depends on radar resolution. Under some conditions the component B_i may be made up of both the Bragg scattered return and unresolved spikes. However, S_i is only the spatially resolved spike component.

Estimations from data recorded in the experiment, using one-dimensional samples of $H_i(\mathbf{r})$ and $V_i(\mathbf{r})$, show that the relative fluctuations of the brightness in images of the first type are weak at both polarizations; that is,

$$S_1^H(\mathbf{r}) < B_1^H(\mathbf{r}), \quad S_1^V(\mathbf{r}) < B_1^V(\mathbf{r}). \qquad (3)$$

By virtue of this, we get

$$H_1(\mathbf{r}) \approx B_1^H(\mathbf{r}),\ V_1(\mathbf{r}) \approx B_1^V(\mathbf{r}); \qquad (4)$$

that is, the texture of the images of the first type is formed by the large-scale background components, $B_1^H(\mathbf{r})$ and $B_1^V(\mathbf{r})$, which are strongly correlated (see Figs. 4 and 5a).

In contrast to the first type, images of the second type have mean brightnesses in the HH- and VV-polarized images that are rather similar, and they also look similar. The amplitudes of the spikes in images of the second type are higher than those in images of the first type and are compared with the background amplitudes:

$$S_2^{H,V}(\mathbf{r}) \approx B_2^{H,V}(\mathbf{r}). \qquad (5)$$

Thus, for the brightness of images of the second type, (2) cannot be simplified as it could to produce (4). For the second type of images the locations of the spikes are strongly correlated with the maxima of the background. This is seen on the one-dimensional runs (Fig. 5b).

The images of the third type, presented in Fig. 7a,b and in the one-dimensional runs in Fig. 5c, show that spikes behave differently from images of the first and second types. The VV-polarized images of the third type look like large-scale spatial distributions of a signal associated with large wave systems such as swells, or are produced by spatial variations of the near-water wind field. The presence of spikes with moderate amplitudes on VV-polarized images, regardless of their origin, does not affect the content and texture of the images; it just makes them noisy to some extent. The opposite is true for HH-polarized images of the third type. These images have a marked fluctuating, spiky component dominating their "background" large-scale component image:

$$S_3^H(\mathbf{r}) > B_3^H(\mathbf{r}), \quad S_3^V(\mathbf{r}) < B_3^V(\mathbf{r}). \qquad (6)$$

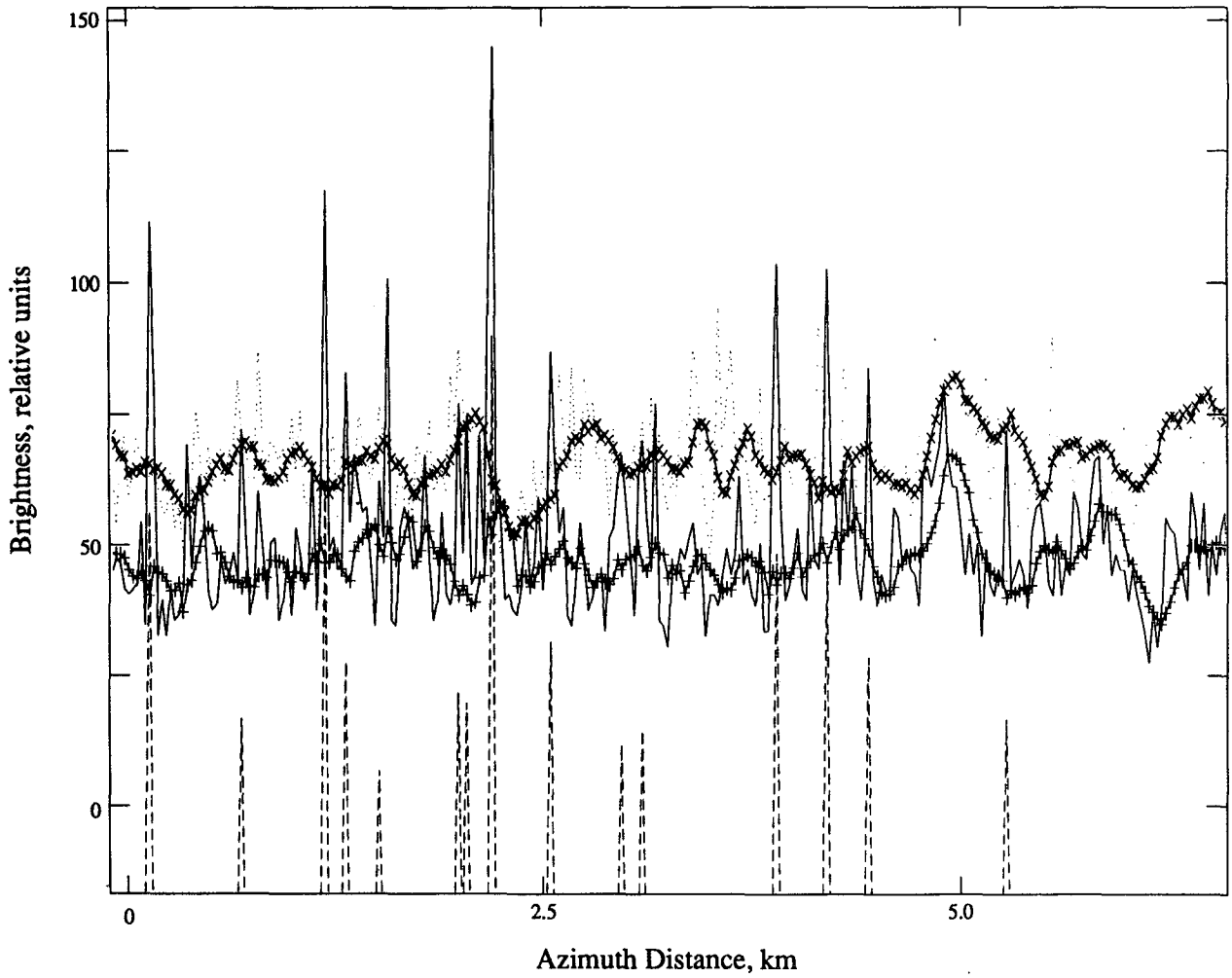

FIG. 8. Radar image brightness for azimuthal HH (solid) and VV (dotted) samples for 21 July; spike positions on the HH sample are shown by the dashed lines at the bottom. Also shown are brightness for the smoothed HH sample with spikes removed (+) and the smoothed VV sample with spikes removed (×).

Therefore, common features related to the background component of the HH-polarized image are weakened compared with the VV-polarized image. At the same time, strong spike clusters with their own texture dominate in HH-polarized images, surpassing all weak details. Because spike clusters in HH-polarized images are not correlated with the dominant background in VV-polarized images, different polarizations produce images with different visual impressions of the same ocean area.

b. One-dimensional statistical analysis

To obtain some quantitative measure of similarity or dissimilarity of the images recorded at different polarizations, we calculated the cross-correlation coefficients between corresponding signals. For this purpose, the data for all three types of images obtained on 16, 21, and 24 July were used. Azimuthal samples of the brightness near the grazing angle $\psi = 17°$ were chosen from HH and VV images of the same areas taken for different environmental conditions. Figure 8 presents an example of the space evolution of the original HH (solid line) and VV (dotted line) signals versus the azimuthal distance on 21 July. To obtain more stationary runs of brightness, we selected the image fragments without internal wave signatures. The grazing angle $\psi = 17°$ was chosen for correlation analysis because it corresponds to the portion of the beam swath closest to the aircraft where the radar resolution of 25 m is the best. First, attention was paid to the correlation between the individual spikes on HH and VV images. Pixel-to-pixel comparison of these images, even with the compensation of the image mismatch mentioned above, shows that the coincidence between spikes at different polarizations is rare. It indicates that spikes are proba-

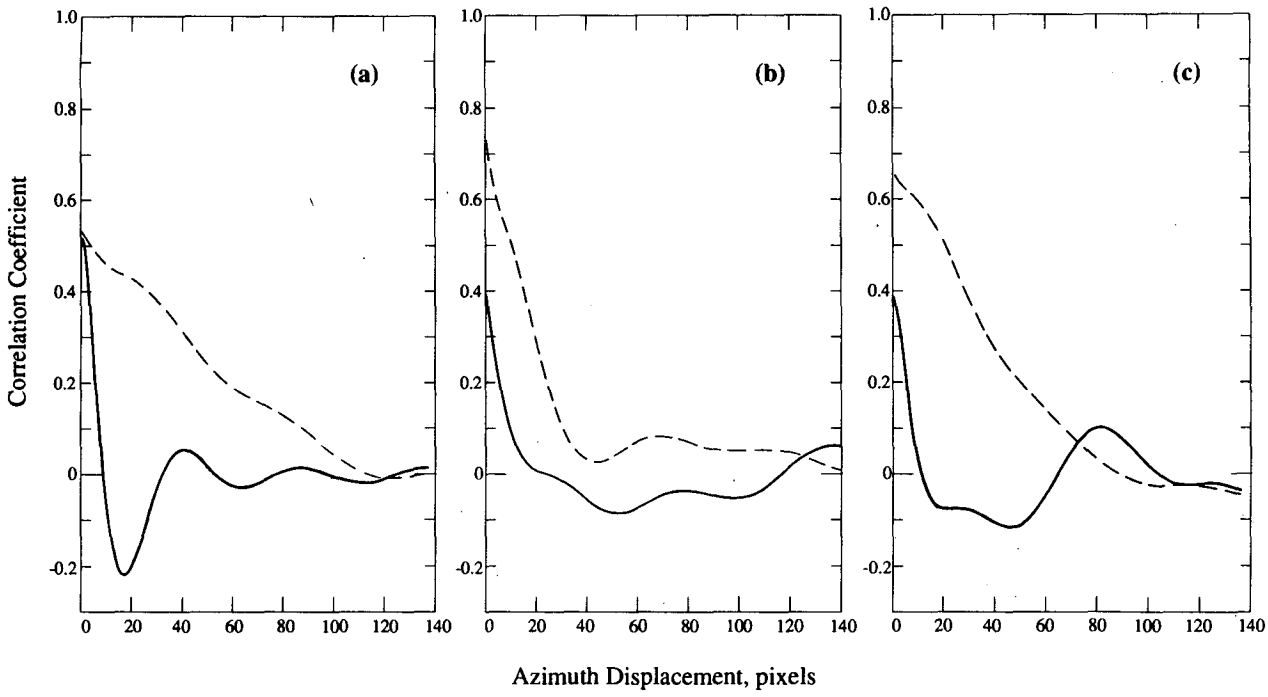

FIG. 9. Spatial correlation between HH and VV samples versus the azimuth displacement: correlation between original samples for HH and VV polarizations (solid) and correlation between the original samples with spikes removed (dashed): (a) type 1 images, (b) type 2 images, and (c) type 3 images.

bly caused by scattering objects having mirrorlike properties. Using the existing angular divergence between the beams of the antenna, one may conclude that the spikes should have a polar diagram width narrower than 1°–2°.

Nevertheless, there are general textural similarities between two images at different polarizations. This is because of the strong correlation between large-scale components, $B_\uparrow^H(\mathbf{r})$ and $B_\uparrow^V(\mathbf{r})$. To deal with large-scale components, we subjected the original signal to a cutoff of significant spikes and further spatial smoothing. This smoothing excluded the residual high-frequency image component.

The azimuthal traces taken at 1 km from the nearest edge of the image were chosen for the processing because the smallest spatial difference between the beams for the two polarizations ensures the minimum time delay in this region. Spikes were cut off from the original samples using a procedure similar to that described by Jessup et al. (1991). The following criteria (physical rather than statistical) were applied for the selection of significant (in a sense) spikes. A significant spike was that burst 1) whose magnitude exceeded some physically meaningful threshold and 2) whose width, determined as a distance between side minima, was small enough (less than five pixels). The threshold over the average signal for both polarizations was chosen to be the difference between average levels of HH and VV signals. (The averaging was performed over the sliding 101-pixel window.) Such a choice of threshold makes it more probable that selected bursts are a result of some non-Bragg mechanisms (say, a quasi-specular reflection from steep breakers) rather than a local increasing of the signal due to the Bragg scattering. Indeed, as was pointed out above, for Bragg scattering the VV component of the signal should be stronger than the HH component. At the same time, a quasi-specular reflection should produce spikes with the same amplitude for both polarizations, which justifies the choice of the same threshold over a corresponding average for both polarizations.

For example, a threshold of 25 relative units was determined for the first type of images. The bottom dashed lines in Fig. 8 represent the positions of those spikes (exceeding this threshold and having a width of less than five pixels) taken from the original HH sample. The same procedure with the same threshold was applied for the spike cutoff from the original VV signals. The further smoothing procedure was performed using spatial averaging over a 7 × 7 pixel square in the azimuthal and range directions, and it corresponds to a 175 m × 175 m square on the ocean surface. This procedure was applied both to the original samples having a length of 914 pixels in the azimuthal direction and to the same signal with significant spikes removed. Two curves in Fig. 8 correspond to those smoothed for HH (marked by +) and VV signals (marked by ×) with significant spikes removed.

Figures 9a–c illustrate computed correlation coefficients for the ith type of image versus azimuth lag, or displacement Δx:

$$\beta_i^2(\Delta x) = \frac{\langle H_i(x, y)V_i(x + \Delta x, y)\rangle - \langle H_i(x, y)\rangle\langle V_i(x, y)\rangle}{\sqrt{\langle H_i^2(x, y)\rangle - \langle H_i(x, y)\rangle^2} \times \sqrt{\langle V_i^2(x, y)\rangle - \langle V_i(x, y)\rangle^2}}, \quad (7)$$

where angular brackets mean a spatial averaging over 914 pixels in the x direction and 7 pixels in the y direction. For simplicity's sake, random fields H_i and V_i are assumed to be statistically homogeneous. Figures 9a–c show spatial correlation functions for image types 1–3, respectively. The solid curves represent the correlations between original raw samples for HH and VV polarizations. The dashed curves show HH–VV correlation coefficients after the spikes were cut off of the original HH and VV samples. The correlation curves for the second and third types of images in Figs. 9b,c are for different wind speeds, 10 m s^{-1} and 7.5 m s^{-1}, respectively, and for unstable atmospheric conditions.

The comparison of shapes of all three solid curves in Fig. 9 demonstrates that the minimal correlation lengths are about five pixels, which are related to spike spatial width. Corresponding spike-removed correlations (dashed curves) show larger correlation lengths, which is consistent with the large-scale structure of the background component. Different values of correlation length, from 20 pixels for Fig. 9b to 50 pixels for Fig. 9a reflect the diversity of large-scale textures.

The correlation coefficient at zero-lag for the first type of image (solid curve in Fig. 9a) is 0.53, which is higher than for the other types of images. After removing the spikes (dashed curves), we see that the zero-lag value of correlations for the first type increases insignificantly, whereas for the other types (Fig. 9b,c) this value is 0.73 and 0.65, respectively.

Estimations of correlation coefficients by Eq. (7), using Eq. (2), give some ideas about possible interpretation of the curves obtained. The close zero-lag values of about 0.5 for both curves in Fig. 9a occur if 1) the mean level for the HH background is much lower than for the VV background (that complies with the Bragg model for background signals) and 2) both the zero-lag correlation between HH and VV backgrounds and the zero-lag correlation between HH and VV spikes are high enough and close to 0.5. This situation can occur for images of the first type, which indeed have a larger degree of similarity between spatial structures at HH and VV polarizations than do the second and third types.

For Figs. 9b,c the situation is different. The higher zero-lag values for the spike-removed correlations mean that 1) HH and VV spikes are higher above background level than for the case of Fig. 9a, but they do not correlate with each other as much as in the case of Fig. 9a, and 2) the backgrounds at different polarizations are highly correlated. Because of this, the procedure of spike cutoff increases the zero-lag value of corresponding correlations.

Therefore, one may conclude that for all three types of images the spatial variations of the background of one-dimensional radar signals at two polarizations show a meaningful correlation. Second, the spikes are an important feature for all types of images, but with various statistical properties. Third, the study of the behavior of zero-lag correlations allows us to identify the first type of images. At the same time, the statistical analysis undertaken did not help us to separate the second and third types. Probably, for this purpose one should invoke a two-dimensional statistical analysis. However, the spatial discrepancy between the beams for each polarization (Fig. 2) prevents us from making such an analysis with high enough accuracy.

c. *Comparison with the two-scale Bragg model*

Radar backscattering from the ocean surface for wavelengths of the X band and shorter waves at grazing angles less than 20° remains a poorly understood phenomenon despite considerable efforts both in experiment and theory. At the same time, it is known that the backscattering signal, which is obtained for longer radar wavelengths and steeper incidence, is significantly less spiky and complies rather well with the two-scale Bragg model (Valenzuela 1978). According to this model, spatial variations of the image brightness may occur because of spatial variations in either the ripple amplitude or the facet local tilts, or a combination of these two mechanisms. Alpers et al. (1981) showed that for images of ripples tilt modulated with long gravity waves, the only differences between the two polarizations are that 1) the tilt modulation of the image brightness is greater for HH polarization than for VV polarization and 2) the image brightness itself is less for HH polarization than for VV polarization. This model might be expected to provide only some trends for background components at both horizontal and vertical polarizations for the K_u-band radar and grazing angles less than 20°.

It is difficult to make a direct comparison here between two-scale results and measured brightnesses because of calibration problems. Nevertheless, the images of the first type follow the results of two-scale theory at least qualitatively, and they can be treated as the spatially distributed return caused mainly by the Bragg resonant mechanism with a minor influence of sea spikes. The absence of significant fluctuations (spikes) on VV-polarized images of the first type means that the received signal is averaged sufficiently over both the ripple statistics and the tilt statistics of the modulating waves having horizontal scales less than the pixel size, that is, 25 m. Another indication that images of the first type follow the two-scale theory is the small brightness variations from one pixel to another. Visual spatial

variations of image brightness having scales much larger than one pixel reflect the spatial variability of the ripple field and wave tilts with scales larger than 25 m. The cross correlation between HH and VV images appears to be the highest for the first among the three types (see Fig. 9).

In the case of images of the second type the level of the signal rises. It is very likely that some areas of the spikes, because of their high spatial density, are not resolved by the radar footprint and contribute to the continuous background. The overall correlation between signals at different polarizations remains rather high, producing the similarity between HH and VV images; however, as seen in Figs. 5b and 8, $B_2^H(\mathbf{r})$ sometimes exceeds $B_2^V(\mathbf{r})$. [The two-scale Bragg model cannot predict such a ratio between the levels of the background components $B_2^H(\mathbf{r})$ and $B_2^V(\mathbf{r})$.]

The case of images of the third type is most peculiar. The visual difference between images at the two polarizations is very pronounced (see Fig. 7). The processing of these images supports this observation by showing that the correlation between the total image brightnesses at the two polarizations is low, near 0.4. The two-scale model again fails to predict these differences between images at the two polarizations. Furthermore, the non-Bragg scattering for HH-polarized signals is apparent because of the spike's domination, $S_3^H(\mathbf{r}) > B_3^H(\mathbf{r})$.

5. Interpretation and discussion

The importance of wave breaking for microwave backscattering is widely recognized (see, e.g., Phillips 1988; Wetzel 1990), but the problem of describing the wave-breaking process quantitatively still remains unsolved. Despite the complexity of the problem, it is worthwhile to discuss here the air–sea conditions typical for this experiment and how these conditions may affect the wave-breaking process. We make the clear assumption now that three different types of images correspond to different types of surfaces with specific wind–wave coupling conditions. The common property for the first two types of surface is that the atmosphere in the near-surface layer had a stable or neutral temperature stratification. Under these conditions, the near-surface wind usually has a stable direction and strength that, in the case of an open sea, may produce a large fetch with long quasi-periodic gravity waves having wavelengths of tens of meters.

When the near-surface wind is light, about 3–7 m s^{-1}, the first type of surface occurs, with capillary ripples slightly modulated by large-scale gravity waves or swell, which can be easily resolved by RAR. The presence of a small number of spikes is possible even in this case (Fig. 4). Apparently, these spikes are caused by the steepening and breaking of short gravity waves in a field of near-surface currents caused by internal waves.

The sea surface of the second type can be characterized by a more well-developed sea state, when multiple, plunging events related to breaking crests of large-scale waves are typical. Indeed, the higher friction velocity was observed primarily for the second type of sea surface. The Bragg scattering from ripples gives a background component for the VV-polarized signal, which is strongly correlated with crest-situated, breaker-generated spikes that dominate at HH polarization.

The third type of surface is described differently from the surface of the first and second types mainly because of the specific wind–wave coupling regime caused by unstable stratification in the near-surface atmospheric layer. This regime is characterized by a moderate mean wind speed and, at the same time, by a high spatial variability of wind speed and direction due to the unstable, turbulent atmosphere. Recent investigations (Smith et al. 1992) found that young-wind seas are associated with significantly higher drag coefficients than old-wind seas. It was also found that a ripple propagating along the crests of gravity waves produces multiple microscale (centimeters to tens of centimeters) breaking events (Banner and Peregrine 1993). Therefore, we may imagine the following picture of the sea surface of the third type. Because of turbulence that modulates the mean wind, the wind–wave interaction imprints the ocean surface in the form of large-scale cells (of the order of 300–3000 m). These cells contain wind-generated ripples, which, because of Bragg-resonant scattering, are quite visible in the VV-polarized images of the third type (Fig. 7b). At the same time, multiple microscale breaking events produce additional scattering effects that are responsible for the spiky character of HH-polarized images (Fig. 7a).

In this regard it is worthwhile to relate our results to a theoretical model suggested by Phillips (1988). According to him, the normalized backscattering cross section can be represented as the sum of the Bragg contribution and the spike contribution:

$$\sigma_0 = \sigma_B + \sigma_{SS} = A(\theta, \phi)F_1(\theta)\left(\frac{u_*^2 k_0}{g}\right)^{1/2} + F_2(\theta, \phi)\left(\frac{u_*^2 k_0}{g}\right)^{3/2}, \quad (8)$$

where A, F_1, and F_2 are some angular dependencies, which for our consideration can be treated as constants. Equation (8) yields for the spike/background ratio:

$$\frac{\sigma_{SS}}{\sigma_B} = \frac{F_2(\theta, \phi)}{A(\theta, \phi)F_1(\theta)}\left(\frac{u_*^2 k_0}{g}\right). \quad (9)$$

Table 2 summarizes environmental conditions for observations of each type of RAR image and provides a comparison of the Phillips scaling parameter $P = (u_*^2 k_0)/g$ with measured values of the ratio σ_{SS}/σ_B for each polarization and each type of image. One can

TABLE 2. Environmental conditions that are favorable (*F*), unfavorable (*U*), or indifferent (*I*) for observations of the three types of RAR images (see Table 1), spike/background ratios, and Phillips parameter (*P*).

Conditions	Type 1	Type 2	Type 3
Hydrophysical conditions			
Seasonal thermocline	*I*	*I*	*F*
Internal waves	*I*	*I*	*I*
Atmospheric stratification			
Neutral	*I*	*I*	*I*
Stable	*F*	*F*	*U*
Unstable	*U*	*U*	*F*
Wind conditions			
Weak (0–7 m s^{-1})	*F*	*U*	*I*
Steady ($\geq$10 m s^{-1})	*U*	*F*	*U*
Variable (4–14 m s^{-1})	*U*	*U*	*F*
Surface conditions			
Ripple	*F*	*F*	*F*
Short steep waves	*U*	*I*	*F*
Large wind waves	*U*	*F*	*I*
Swell	*I*	*I*	*I*
Large plungings	*U*	*F*	*I*
Small spillings	*I*	*I*	*F*
Microscale breakings	*I*	*I*	*F*
Spike/background ratio			
HH	<1	~1	>1
VV	<1	~1	<1
Phillips parameter, (*P*)	1–1.2	1.6–2	2–2.2

see that there is strict correlation between measured values and P, except for the case of VV polarization of the third type. The dimensionless parameter $(u_*^2 k_0/g)$ for the third type reaches about 2.2, while for the first and second types the value of this parameter is correspondingly about 1.2 and 1.6. According to Phillips (1988), when this parameter exceeds 2, the physics of the surface involved in the Bragg returns becomes very sophisticated. Because the saturation range of the wind–wave spectrum exists only for gravity-capillary waves, the radar VV-polarized returns that are primarily from sea ripples might reach a saturation region, while the portion of HH-polarized returns that are associated with breaking waves at all scales can overtake VV-polarized radar sea returns. The ratio between HH- and VV-polarized returns from young-wind seas increases compared with the ratio for the first and even second types.

Therefore, the specific wind–wave coupling regime caused by unstable stratification in the near-surface atmospheric layer might explain a peculiar polarization behavior of the K_u-band RAR images of the third type. If the heat flux through the sea surface is held constant, then the air–sea temperature difference decreases as the wave amplitude increases. Moreover, if radiation and evaporation dominate surface cooling, then the average heat flux with waves usually exceeds that without waves. A measure of these changes was called the "wave effectiveness" by Witting (1971). The capillary waves near 1-cm wavelength (these capillary waves are the resonant components for our K_u-band radar) can decrease mean temperature gradients by a factor of as much as 9 if the average heat flux at the sea surface does not depend on the presence of the waves. Over land, the air–land temperature difference can be quite large, and consequently the surface buoyancy flux is often large. The surface buoyancy flux over the sea is relatively small because the air–sea temperature and vapor pressure differences are small. It is reasonable to expect that the growth rate of capillary waves in the presence of a thermal boundary on the sea surface will be different compared with the rate during stable atmospheric conditions. This suggests that the measurements using K_u-band radar with low grazing angles could evaluate these effects as they pertain to the observation of fluctuations in ocean backscatter returns caused by surface layer instability. Valenzuela (1978), who used the term "anomalous" conditions when discussing experimental scatterometric data, recognized the possible influence of the atmospheric factor on microwave radar scatter from the sea surface at grazing angles.

6. Summary and conclusions

The main focus of the Joint U.S.–Russia Internal Wave Remote Sensing Experiment was a study of the internal wave field in the New York Bight region used previously in 1984 for the SAR Internal Wave Signature Experiment. However, we chose another aspect for our consideration, namely, the observable differences in RAR images obtained with horizontal and vertical polarizations at relatively low grazing angles. Our purpose is to demonstrate that this difference in images appears during unstable atmospheric conditions. The image brightness is assumed to be divided into two different dynamical components, the continuous background and fluctuating spikes. The background is represented mainly by the Bragg-resonant scattering from wind ripples and spikes that are the result of backscattering from steep, sharp-crested, or breaking waves. Spikes are a very important component in explaining some peculiarities of dual-polarized radar imagery. The Phillips dimensionless parameter $(u_*^2 k_0/g)$ for the radar cross section can be applicable for the analysis of radar data at low grazing angles.

The RAR images obtained can be classified into three types, which correspond to three types of ocean surfaces. The first type complies qualitatively with predictions of the two-scale Bragg model and is related to weak sea states and stable atmospheric conditions. The second type has a significant spike contribution at both polarizations, which correlates with the image background and is related to moderated sea states and stable or neutral atmospheric conditions. The third type, which shows a dissimilarity between RAR images at different polarizations, can be described by spikes at the HH polarization produced by

the individual deep-water breaking gravity waves and the background at the VV polarization produced mostly by Bragg scattering from ripples generated by local winds. These two components are almost uncorrelated because of the specific mechanism of wave breaking in this case that develops under unstable atmospheric conditions.

The polarimetric RAR imagery at grazing angles can provide additional useful information about air–sea conditions, and particularly about the atmospheric stability near an ocean surface and wave-breaking processes. For further advances, a technique must be developed for measuring the breaking events and the capillary wave spectrum by means of both direct and remote sensing methods for the statistical quantification of breaking in the wind wave spectrum and for the study of backscattering mechanisms.

Acknowledgments. We thank the crew of the Russian aircraft TU-134 for its cooperation throughout the airborne survey and the team of the *Academic Ioffe* for supplying us with in situ data. We thank Steven Clifford and James Churnside of the Environmental Technology Laboratory of the National Oceanic and Atmospheric Administration, and Richard Gasparovic of The Johns Hopkins University/Applied Physics Laboratory for helpful discussions. The authors gratefully acknowledge the reviewers, whose comments and constructive suggestions resulted in major improvements to the initial version of this paper. This work was supported by the Environmental Technology Laboratory of the National Oceanic and Atmospheric Administration. This paper has been generated as part of a joint NOAA/DOD–Advanced Sensor Applications Program.

REFERENCES

Alpers, W. R., D. B. Ross, and C. L. Rufenach, 1981: On the detectability of ocean surface waves by real and synthetic aperture radar. *J. Geophys. Res.*, **86,** 6481–6498.

Anthes, R. A., E.-Y. Hsie, and Y.-H. Kuo, 1987: Description of the Penn State/NCAR Mesoscale Model Version 4 (MM4). NCAR/TN-282+STR, National Center for Atmospheric Research, 66 pp.

Banner, M. L., and D. H. Peregrine, 1993: Wave breaking in deep water. *Annu. Rev. Fluid Mech.*, **25,** 373–397.

Gasparovic, R. F., J. R. Apel, and E. S. Kasischke, 1988: An overview of the SAR Internal Wave Signature Experiment. *J. Geophys. Res.*, **93,** 12 304–12 316.

Guinard, N. W., J. T. Ransone Jr., and J. C. Daley, 1971: Variation of the NRCS of the sea with increasing roughness. *J. Geophys. Res.*, **76,** 1525–1538.

Jessup, A. T., W. C. Keller, and W. K. Melville, 1991: Measurements of sea spikes in microwave backscatter at moderate incidence. *J. Geophys. Res.*, **95**(C6), 9679–9688.

Lavrova, O. Y., A. D. Rozenberg, and A. V. Smirnov, 1991: Measurement of the spatial spectra of a disturbance using aircraft side-looking radar. *Sov. J. Remote Sens.*, **9,** 374–390.

Phillips, O. M., 1988: Radar returns from the sea surface: Bragg scattering and breaking waves. *J. Phys. Oceanogr.*, **18,** 1065–1074.

Smirnov, A. V., and V. V. Yakovlev, 1992: Study of ocean surface features observed with airborne RAR and SAR ALMAZ-1 satellite. *IGARSS '92—International Space Year: Space Remote Sensing,* IEEE, 471–473.

Smith, S. D., R. J. Anderson, W. A. Oost, C. Kraan, N. Maat, J. DeCosmo, K. B. Katsaros, K. L. Davidson, K. Bumke, L. Hasse, and H. M. Chadwick, 1992: Sea surface wind stress and drag coefficients: The HEXOS results. *Bound.-Layer Meteor.*, **60,** 109–142.

Trizna, D. B., 1991: Statistics of low grazing angle radar sea scatter for moderate and fully developed ocean waves. *IEEE Trans. Antennas Propag.*, **39,** 1681–1690.

Valenzuela, G. R., 1978: Theories for the interaction of electromagnetic and oceanic waves—A review. *Bound.-Layer Meteor.*, **13,** 61–85.

Wetzel, L. B., 1990: Electromagnetic scattering from the sea at low grazing angles. *Surface Waves and Fluxes,* Vol. 2, G. L. Geernaert and W. L. Plant, Eds., Kluwer Academic, 109–171.

Witting, J., 1971: Effects of plane progressive irrotational waves on thermal boundary layers. *J. Fluid Mech.*, **50,** 321–334.